

DESIGN AND TESTING OF EXTERNALLY FINNED TUBE CAVITY RECEIVER FOR BRAYTON CYCLE PREHEATING PURPOSES

Elias J.J. Basson¹, J.E. Hoffmann², and A.B. Sebitosi²

¹ Solar Thermal Energy Research Group, University of Stellenbosch; concentrating.sun.ac.za

University Of Stellenbosch; Stellenbosch, 7600, South Africa, 071 9099 587, 17495644@sun.ac.za

² University of Stellenbosch; Stellenbosch, 7600, South Africa

Abstract

The Hybrid Pressure Air Receiver (HPAR), proposed and investigated by Kretzschmar [1] and further work done by Heller [2], is a novel metallic tubular volumetric open cavity concentrated solar power receiver that makes use of staggered tubes to create a macro cavity effect. In this study the effects of external radial fins on the receiver tubes are investigated.

The hypothesis is that the micro cavities, created by the fins, and the air movement through the fins will distribute surface heat towards the shadow side of the tubes. This is expected to reduce the temperature gradient and thermal stresses on a receiver tube circumference. By removing heat from the external and internal surfaces of the metal tubes the operating temperature range of metal heat exchangers can safely be extended to the material limits. Furthermore, the addition of external fins is expected to increase the external flow mixing and thereby create a more uniform cavity temperature distribution.

An experimental investigation will be conducted on the designed receiver. Thermocouples are placed at various positions to capture the thermal behaviour of the receiver. At this stage a non-validated model, predicting the behaviour, is presented. At the time of the conference experimental data is expected to be available.

Keywords: CSP; Tubular Receiver; HPAR; Brayton cycle; finned

1. Introduction

The need for more cost effective and scalable concentrated solar power systems exists in the energy market. This paper aims to investigate the radiation trapping effectiveness of a cost effective solar heat exchanger to be used at various scales of electricity production.

The receiver being investigated can be described as a staggered externally finned tube open volumetric cavity receiver based on various receiver technologies that utilises air as working fluid. Air is drawn into the cavity to capture the external convective

losses and in the process moves heat deeper into the cavity, where losses are less dominant.

The temperature distribution on the circumference of selected tubes in the depth of the cavity, as well as the cavity temperature distribution, may provide a measure of the effectiveness of the addition of external fins. The thermodynamic efficiency, of the receiver, will be a secondary validation of the enhancement of the concept, in this investigation the receiver was not optimized for maximum thermodynamic efficiency.

1.1 Background

Solar thermal energy provides a novel and cost competitive energy storage ability, which enables the dispatchability of energy to match the grid demand and thus provide baseline electricity on demand, something that other renewable energy sources can only do at a greater cost. In a bid to further decrease the levelised cost of electricity (LCOE), research at Stellenbosch University is focussing on using air as working fluid for combined cycle co-firing Concentrated Solar Power (CSP) plants.

Initially proposed by Kröger in 2011 [3] the SUNSPOT (Stellenbosch University Solar Power Thermodynamic) cycle is a combined cycle CSP plant which uses a rock bed as thermal energy storage. Figure 1 (below), shows the cycle layout. Heller [2] identified that the turbine of the Brayton cycle is a bottle neck which limits the charging rate of the TES (thermal energy storage). This limits the quantity of dispatchable energy to be stored and later used by the Rankine cycle. Heller [2] proposed the so-called SUNDISC (Stellenbosch University Direct Storage Charging Dual Pressure Air Receiver) cycle, to overcome the SUNSPOT shortcomings in terms of TES charging rate, which is expected to improve the dispatchability and baseload delivery capability.

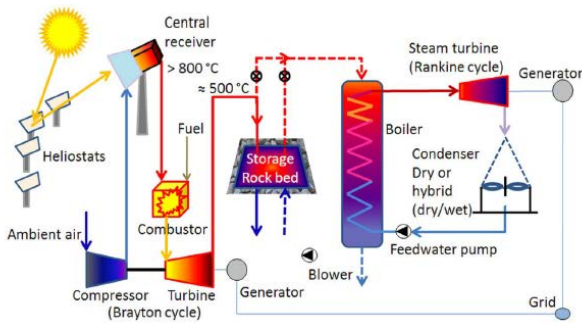


Figure 1: Schematic of the SUNSPOT cycle [2]

The dual pressure air receiver, as proposed by Heller, would allow for the TES to be charged throughout the day, while the Brayton cycle is operating at full capacity, by charging directly from the low pressure receiver and the exhaust of the Brayton cycle. Figure 2 shows the layout of the proposed SUNDISC cycle.

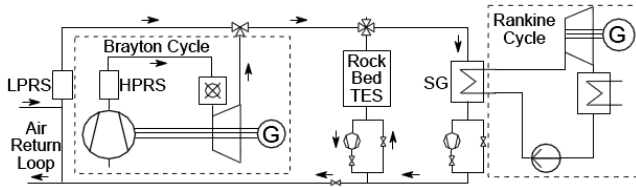


Figure 2: Schematic of SUNDISC cycle [2]

The dual pressure air receiver has to be able to satisfy the fluid temperature requirements of the Brayton cycle and the TES. The goals set by Heller [2] were 800 °C for the Brayton cycle and 524 °C for the TES. However, during simulation, the goal for the TES charging fluid temperature could not be achieved. Heller suggested the addition of external fins to the receiver tubes, to further increase the heat transfer to the TES charging fluid. The increase in energy transfer to the low pressure air stream is directly related to a decrease in energy transfer to the high pressure air stream.

The nature of the incident radiation, falling unidirectional onto the tubes, is a challenge for tubular receiver systems and even more for receivers using working fluids with low thermal capacity. Research has been done on various strategies to distribute the tube surface temperature for more uniform heat transfer and less thermal stress. This is partially achieved by internal and external enhancements. The use of twisted tapes, wire coils and other similar passive heat transfer enhancements on the inside of the tubes show promising results [4].

For the SOLHYCO project of the DLR, innovative Profiled Multi-Layer tubes was developed to reduce the temperature difference on the circumference of the tube and thereby increase the heat transfer. These tubes consisted of an Inconel outer, a copper middle layer and an Inconel inner layer. The high conductivity of the copper was used to reduce the

circumferential temperature. During tests the circumferential tube temperature difference was reduced to within 80.9% of the front temperature. However during these tests the thermal cycling damaged the intermetallic connection and as a result the tubes were never used in a receiver according to the final report summary [5].

1.2. The modified Hybrid Pressurised Air Receiver (HPAR)

The so-called modified HPAR concept is based on the work done by Kretzschmar et al. [1] and modified by Heller [2] based on the limitations thereof. Figure 3 below depicts the layout and workings of such a concept. Tubes are arranged staggered in a cavity to form macro cavity effects, which aims to trap the incident radiation by reflectance into the depth of the cavity.

The main goal of such a receiver is to transfer heat to the internal pressurised fluid as a pre-heating stage for the Brayton cycle. Charging of the TES and other high temperature low pressure air applications such as pre-heating are a secondary goal.

Tubes at the aperture experience the highest heat flux and largest radiative losses due to the large view factor to ambient. In a bid to decrease the losses to ambient, and thereby increase the thermodynamic efficiency of the receiver, efficient operating strategies and enhancements are required.

The biggest thermal loss, at high temperatures, is radiative losses to the environment, which is a function of the 4th order of the temperature difference between tube wall temperature and the environment. In order to reduce these losses, ideally the coolest pressurised air is piped through the front rows of the receiver first to decrease the surface temperature, from there it moves deeper into the cavity supporting the volumetric effect [2].

The novel idea of the HPAR is to draw air into the depth of the cavity. This reduces the surface temperature of tubes with the highest view factor to ambient by means of forced convection.

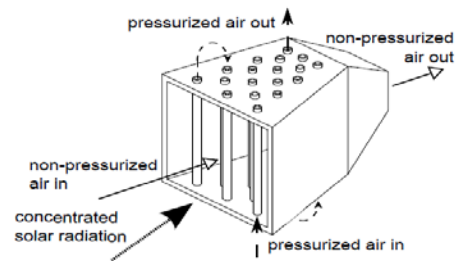


Figure 3: Sketch of the HPAR concept [2]

The HPAR is essentially a combination of tubular and open volumetric receivers. However, the limitations of both tubular

and volumetric receivers are still present in this combined receiver, namely the circumferential temperature gradient on the tubes, leading to inhomogeneous expansion and therefore thermal stress and the non-homogeneous heating, of the fluid in a volumetric receiver, as the flow follows the path of least resistance resulting in cool and hot spots.

For the modified HPAR concept it was attempted to address these limitations mentioned above by active and passive methods [2]. To reduce the thermal losses, active enhancements such as operating strategies were investigated, as well as various passive enhancements such as internal heat transfer enhancements that disturb the flow boundary layer. External enhancements, such as the addition of radial fins, which increase the heat transfer surface area, and cavity enhancements, such as the addition of quartz prisms or windows at the aperture, to reduce the view factors.

2. Method

This study aims to experimentally investigate the effect of radial external fins on the solar radiation heat trapping abilities of metal tubes. The experimental investigation can be used to validate theoretical models of tubular CSP receivers.

The external fins are expected to enhance the heat trapping capabilities in various ways. The micro cavity and ratio between the fin spacing and height is designed to recapture radiative losses, which can be conducted to the inside and to the shadow side of the tube. Further, when air is drawn over the finned tubes, the potential convective losses are used to move energy deeper into the cavity where it can be regained, thereby increasing the heat harnessing efficiency of the receiver by some extent.

A theoretical 1-D model of the receiver was generated in MatLab using heat transfer theory for the convection, conduction and radiation heat transfer. Based on a list of assumptions a prediction of system behaviour was generated, stating the temperature distribution based on the input and geometry conditions. At this stage the validity of these assumptions could not be checked as the preliminary results are not yet in. The level of detail used for these various energy transfer mechanisms are important.

Figure 4 illustrates the layout of the test receiver to be built and the basic tube geometry. The first two columns are arranged staggered, to block the view factor to ambient of the other tubes behind them. Columns 3-7 are spaced to allow deeper penetration of radiation. The spacing also allows for channelling of the flow in a converging nature to increase the forced convective heat transfer and flow mixing. The tubes set to be evaluated in the 1-D models are indicated in figure 4 and was chosen to represent a pattern that can be propagated in a

360° field application, as proposed by Heller [2]. The chosen fin to tube diameter ratio is 1.8, due to material limitations.

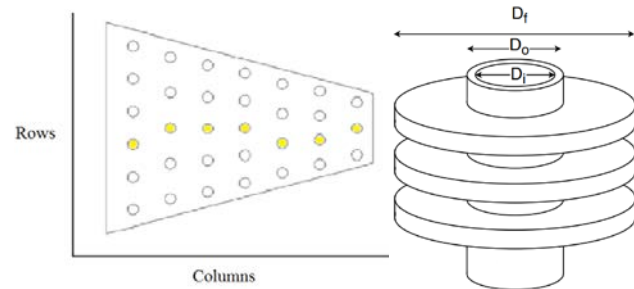


Figure 4: Receiver tube layout and fin geometry

3. Models

In order to model the thermal behaviour of the receiver in question an extensive energy balance needs to be done focussing on the following energy transfer mechanisms:

- Solar radiation absorption and reflection
- Internal forced convection to the internal fluid stream
- External forced convection from the tube and fin surface to the air stream
- Radiation heat transfer between the tubes, fins and the environment.
- Conductive heat transfer in the metal tube and fin circumference

List of assumptions for 1-D model

- No axial conduction and axis-symmetric tube wall temperature
- The 7 tubes are arranged in a row with no offset
- Radiative heat transfer between tubes cancel out
- The cavity walls do not participate in the heat transfer
- Non-pressurized air temperature is perfectly mixed after each tube row
- Incident radiation is absorbed on a cylinder with the finned diameter (diameter of the fin tip, see figure 4), or an approximation based on the geometry
- The finned tubes are modelled as a cylinder with larger surface area to convection than to radiation
- Fin efficiency is incorporated to account for conduction to the internal fluid
- No temperature losses occurs in the manifold system

All of these models will be discussed briefly in this section and the results thereof will be discussed later.

3.1 Central Mathematical Model

Three models were created. One reads in ray tracing data on the tube surfaces and the other two read DNI data and models the heliostat field efficiency to approximate the incident radiation

on different areas. In this section the central mathematical model is discussed followed by the individual models, each model modifies the theory to satisfy its assumptions, in the following sections. Due to safety concerns the planned experiment will use water as internal fluid and therefore the models will also include this. For all of the models the view factor of the chosen row of tubes to the environment was generated with the S2S radiation model in Ansys Fluent 18.2.

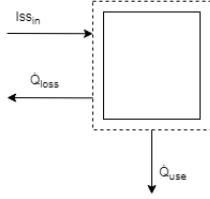


Figure 5: Control volumes with external energy balance

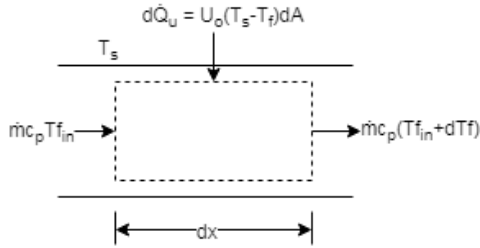


Figure 6: Control volumes of the internal energy balance and energy transfer

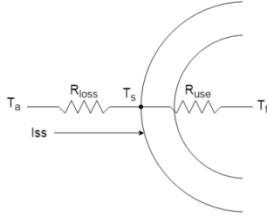


Figure 7: Global thermal resistance diagram

For the 1-D model the energy balance on the control volume is summed, as figure 5 depicts, based on published work [1,6]. The energy transferred to the internal working fluid is termed the used energy, as it is transported from one control volume to the next. The heat loss is a function of the surface temperature and the external air temperature. A loss coefficient is approximated based on the convective and radiative losses. The incident solar radiation (ISS) implementation methods described in this section is a function of surface absorptance and reflectance.

$$\dot{Q}_{use} = A_t ISS - \dot{Q}_{loss} \quad (1)$$

$$\dot{Q}_{loss} = U_l A_t (T_s - T_a) \quad (2)$$

$$\dot{Q}_{use} = A_t [ISS - U_l (T_s - T_a)] \quad (3)$$

$$\dot{Q}_{use} = U_{int} A_t (T_s - T_f) \quad (4)$$

The thermal resistance to the internal fluid is defined as an overall internal thermal loss coefficient:

$$U_{int} = \left[\frac{D_o}{h_{fi} D_i} + \frac{(D_o \ln \left(\frac{D_o}{D_i} \right))}{2k} \right]^{-1} \quad (5)$$

The internal heat transfer coefficient for heating fluids, is calculated with the Dittus Boehler equation, based on developed internal pipe flow correlations:

$$Nu = 0.023 Re^{0.8} Pr^{0.4} \quad Nu \text{ for } Re < 2300 \text{ is } 4.63.$$

From the Nusselt number, the internal fluid heat transfer coefficient can be obtained.

$$h_{fi} = \frac{k Nu}{D_i} \quad (6)$$

Simplifying

$$\dot{Q}_{use} = A_t \left[ISS - U_l \left(\left(\frac{\dot{Q}_u}{U_{int} A_t} + T_f \right) - T_a \right) \right] \quad (7)$$

$$\dot{Q}_{use} = A_t F' [ISS - U_l (T_f - T_a)] \quad (8)$$

F' was termed [6] the collector efficiency function

$$F' = \frac{1}{\frac{1}{U_l} + \frac{D_o}{h_{fi} D_i} + \frac{D_o \ln \left(\frac{D_o}{D_i} \right)}{2k}} \quad (9)$$

The energy transport equation, based on the control volume in figure 6, is presented in the following equation which can be simplified by integrating over the boundaries with the presented boundary conditions.

$$\dot{m} c_p \left(\frac{dT_f}{dx} \right) = F' (ISS - U_l (T_f + T_a)) \pi D_o \quad (10)$$

$$\int \frac{1}{\left(\frac{ISS}{U_l} + T_a \right) - T_f} dT_f = \int \frac{F' \pi D_o U_l}{\dot{m} c_p} dx \quad (11)$$

$$T_f(x)|_{x=L} = T_{fo} \quad (12)$$

This allows one to determine the fluid temperature with no knowledge of the surface temperature

$$T_{fo} = - \left[\left(\frac{ISS}{U_l} + T_a \right) - T_{fi} \right] \exp \left(- \frac{F' \pi D_o U_l x}{\dot{m} c_p} \right) + \left(\frac{ISS}{U_l} + T_a \right) \quad (13)$$

Alternatively it can be written as

$$T_{fo} - T_{fi} = \left[\left(\frac{ISS}{U_l} + T_a \right) - T_{fi} \right] \left\{ 1 - \exp \left(- \frac{F' \pi D_o U_l x}{\dot{m} c_p} \right) \right\} \quad (14)$$

Determining the energy transported from the control volume by the internal flow

$$\dot{Q}_{use} = A_t F_R [ISS - U_l (T_{fi} - T_a)] \quad (15)$$

F_R was termed [6] the heat removal factor. This parameter can be used when selecting a heat transfer fluid

$$F_R = \frac{\dot{m}c_p}{U_t A_t} \left\{ 1 - \exp \left(-\frac{F' \pi D_o U_t x}{\dot{m}c_p} \right) \right\} \quad (16)$$

The external losses can be determined with the following equation. This is updated to account for finned tubes with porosity and fin conduction efficiency.

$$\dot{Q}_{loss} = h_w \pi D_o (T_s - T_a) + F_{ij} \sigma \epsilon \pi D_o (T_s^4 - T_{sky}^4) \quad (17)$$

Using the newly obtained energy loss a new overall heat loss coefficient, which includes a small percentage radiative losses based on the viewfactor F_{ij} , can be determined. The set of equations is solved iteratively per control volume until the overall heat loss coefficient converges to within an error margin.

3.2 Ray tracing model

For ray tracing operations and flux distribution estimations Tonatiuh, a Monte Carlo ray tracer for optical simulation of CSP systems by University of Texas at Brownsville, was used. The heliostat field and receiver were modelled with the built in functions. The heliostats were modelled as parabolic rectangles with the focal distance for each heliostat set to be the respective distance to the receiver. Aiming strategies are not part of this investigation and therefore all heliostats were aimed at the centre of the receiver aperture. Heliostat reflectivity was set to be 0.88 which is a conservative value.

The accuracy of the ray tracer, to predict the flux distribution for the site, still needs to be validated. Tonatiuh has been compared to SolTrace and presented at the 2009 SolarPaces international symposium. According to Blanco et al. [7] the differences over various simulations never exceeded 2.4% and were negligible in most cases.

The following figures illustrate the field layout and ray paths at 15:00 on the 5th of March 2018. Figure 8 illustrates the field layout and figure 9 illustrates the basic receiver constructed from flat and tubular receiver components to represent the test receiver most accurately.

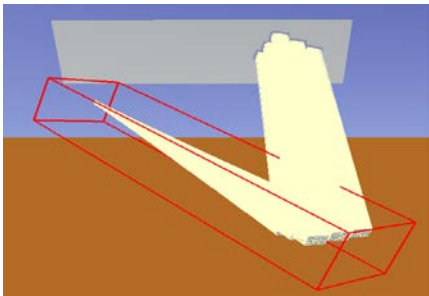


Figure 8: Ray paths and 6 Heliostat field layout

For the receiver tubes the base tube diameter was used and a reflectivity value of 0.1 was chosen, as it best represents the untreated oxidized tubes of the experimental setup. Figure 10

shows the plot of the flux, on the selected tubes to be modelled, generated by this ray tracing exercise which accounts for reflection into the depth of the cavity.

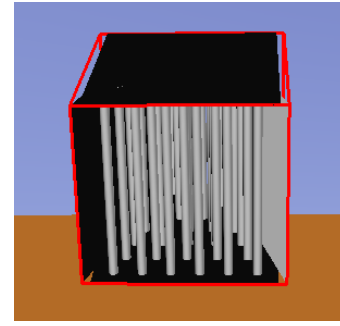


Figure 9: Receiver model on which the flux penetration maps were tested.

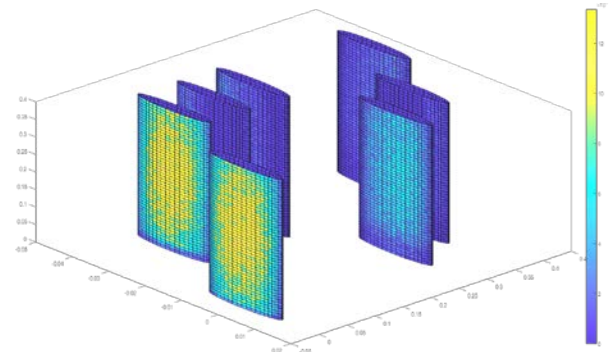


Figure 10: Flux mapping on the selected tubes generated with the ray data from Tonatiuh and plotted in MatLab

3.3 Simulation model with DNI value as input

To account for the unidirectional behaviour of the incident flux distribution it was assumed that the incident flux act on 50% of the external circumferential area of a control volume. This is a crude approximation which most likely under predicts the total incident energy onto the control volumes by omitting reflection effects.

The incident flux distribution and intensity on the aperture is approximated by reading in data from the pyranometer of the Sonbesie weather station on a nearby roof. Hourly and minutely data is freely available and can be used to approximate the operating cycle of the heliostat field throughout the day. This is achieved by modelling the solar position and doing virtual tracking of the heliostats to estimate the cosine losses.

The Helio40 heliostat field is said to have a concentration ratio of 50, however the assumption in the model was that, accounting for losses, the focal point is the size of the aperture. The overall solar field efficiency is determined in the following way and includes the receiver absorption

$$\eta_{SF} = \eta_{ref} \eta_{shade\&block} \eta_{spill} \eta_{cosine} \eta_{absorb}$$

An attempt was made to generate a Gaussian flux distribution on the tubes, but for simplicity it was assumed that the top and bottom 12.5% of the tube length experiences 25 % of the incident flux, thereby creating a step function. To account for the blocking and shading of upstream tubes the incident flux was multiplied by a fraction representative of the tube row number, e.g. row seven receives 1/7 the intensity of the flux at the aperture.

Parameter	Value
η_{reflect}	0.88
$\eta_{\text{shade\&block}}$	0.98
η_{cosine}	0.90
η_{spill}	0.80
η_{absorb}	0.90

Table 1: Input conditions for DNI based heliostat field model

3.4 Simulation model with Raytracing as input

The flux distribution depicted in figure 10 was generated by Tonatiuh. The flux map was exported to MatLab and smoothed with a 5th order polynomial curve fit per row of data, a Fourier series approximation of the circumferential flux distribution was considered as done by Heller [2] but was decided to be unnecessary at this stage. The average circumferential incident flux, on the ray trace discretized height, was calculated from the corresponding smoothed curve. A function of the average incident radiation per height discretization was created along the length of the tube.

From this function the average circumferential incident radiation can be scaled to the discretised volume heights where it was implemented onto the control volume area. This assumption was made to approximate the circumferential flux that represents a normal distribution on the circumference in 1-D.

3.5 Conservative simulation model with different surface areas for the heat transfer modes

For this model the same solar radiation input method was used as in section 3.3, but the incident radiation falls only on an area representative of a perpendicular view of the finned tubes, part base tube circumferential area and part fin tip circumferential area as illustrated in figure 11. For the convective losses the finned area was used, assuming air flow through the fins, thereby increasing the convective heat transfer area. Lastly the radiative loss was assumed to only occur at the fin tips and not the base, as the base radiation was assumed to be trapped by the fins. The area enclosed by the dashed line represents the finned diameter area onto which the incident radiation is implemented in the model discussed 3.3.

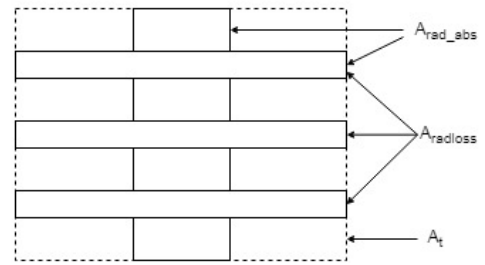


Figure 11: Side view of finned tube

These areas were generated by developing a discrete area ratio of a finned section to an unfinned section and the ratios implemented on the desired control volume size.

3.5 Program structure

Based on the list of assumptions stated three models were generated, namely an optimistic, a conservative and a generic model.

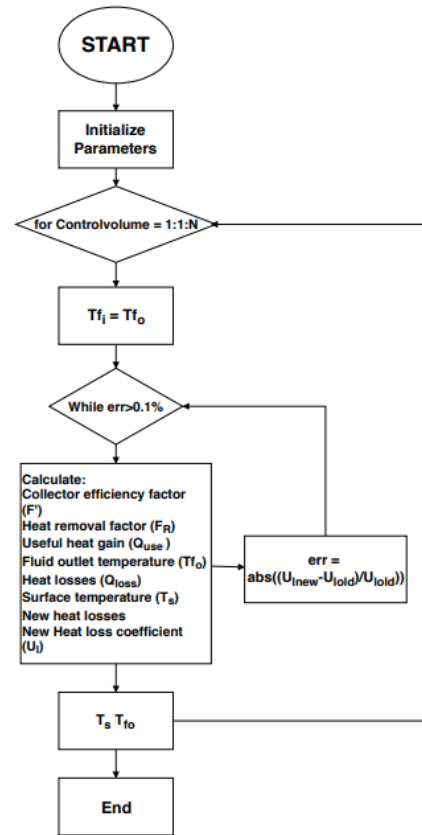


Figure 12: Flow diagram of program solution [1]

All the models solve the set of equations of section 3.1 iteratively. The simulation initialises the parameters, after which it enters a loop that cycle through the control volumes. For each control volume the surface temperature, the fluid temperature and the resulting loss coefficients are solved. The simulation iterates based on an error margin until the temperatures converge and a heat loss coefficient for that

control volume is found. Once convergence is reached the internal fluid temperature is transported to the next control volume and the process repeated. The fluid properties are evaluated in each iteration to describe more accurately the development thereof.

4. Results

For the simulation six heliostats were used to predict the system performance. These six heliostats produced an estimated 1.5 kW input over the simulated aperture area.

For all of the comparative analysis the following inputs were used:

Input	Quantity
\dot{m}_{air}	0.0275 kg/s
\dot{m}_{water}	0.1079 kg/s
DNI	1000 W/m ²

The nature of the chosen receiver geometry design, with the first two columns of tubes in a staggered arrangement as depicted in figure 4, is reflected in the flux data from the ray tracing of the geometry. In figure 13 it can be observed that the surface temperature predictions do not simply reduce towards the back, and that the surface temperature of tube 5 is in fact higher than that of the neighbour tubes based on its location in the cavity. The flux distribution, resembling a Gaussian distribution, can be observed in the temperature distribution along the length of the tubes.

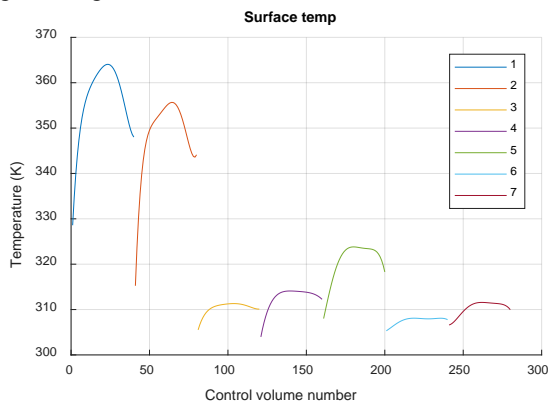


Figure 13: Tube temperature distribution in the receiver depth based on the ray tracing data.

The predicted system temperature distribution for the model with variable areas for the different heat transfer modes is considered the most conservative estimation. At these flow conditions the behaviour of the temperature distribution prediction is similar to the distribution predicted in figure 15. The far smaller radiation absorption area implementation is noticeable in the lower surface temperature estimation.

The surface temperature distribution, in figure 14 & 15, on the tubes based on the field modelling illustrates a stepwise

decrease in surface temperature. The flat peaks are a reflection of the step function flux distribution implemented. The difference in maximum temperature per tube column decrease towards the back reflects the penetration function that is implemented.

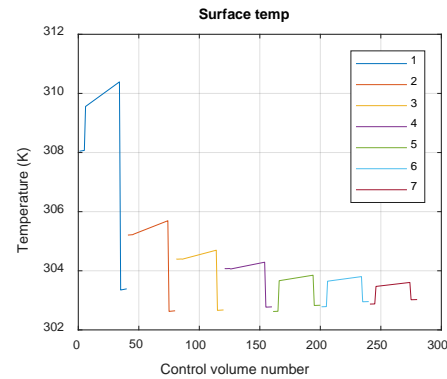


Figure 14: Tube temperature distribution in the receiver depth based on the pyranometer data and the conservative implementation of control volume areas.

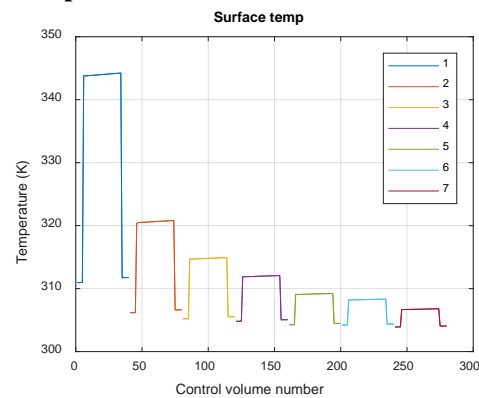


Figure 15: Tube temperature distribution in the receiver depth based on the pyranometer data.

The incident radiation decline implementation method seems to predict reasonable system behaviour when compared to the ray tracing model, but it needs to be validated by the experimental results in the future.

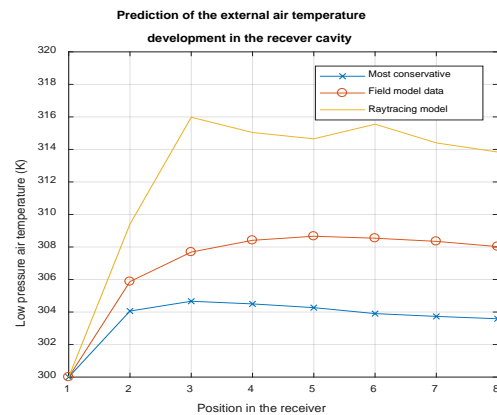


Figure 16: External air temperature development comparison of the models employed

The behaviour of the external fluid temperature distribution prediction in figure 16 relates to the surface temperature distribution plots. The highest gradient occurs at the highest surface temperature. From the behaviour of the Raytracing model, which transfers heat back to the tubes, with surface temperatures lower than the external air temperature it can be interpreted that the model does solve the energy balance correctly.

From all the above simulations the temperature difference between the tube surface and the external fluid is relatively small. This is a direct result of using water, which has a far higher thermal capacity than that of air, as internal fluid. As an exercise the internal fluid was replaced with dry air at 10 bar and 0.0056kg/s. For the same heliostat field input an operational receiver was simulated. The internal air inlet conditions were set to 400 K (compressor outlet temperature).

The surface temperature is depicted with the 7 curves as before, the black line represents the internal pressurised air temperature development in the receiver and the red curve the external fluid temperature. At the outlet the internal and external fluid temperature is close the surface temperature. This is a direct result of the control strategy and the mass flowrates. Higher mass flow rates would increase the energy removal and decrease the temperatures.

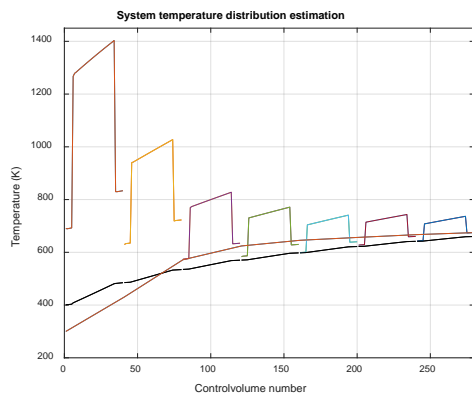


Figure 17: Prediction of system response under Brayton cycle operation conditions

Notably the surface temperature predicted of the first tubes needs to be beyond the material limit in order to produce the desired TES charging outlet temperatures [2] at this flowrate.

In the simulations and the future experiments, the goal is to investigate the effects and effectiveness of the receiver enhancements and not construct a full-scale receiver.

Conclusion

Three theoretical models were constructed to provide an insight into the expected behaviour of the receiver, based on ray tracing incident flux for a specific timestamp and solar field

approximations. The validity of the assumptions is to be evaluated in the future with experimental data. The assumptions and program structure was discussed and the evaluation method laid out.

At this stage a 1-D approach is acceptable to provide reasonable predictions. The validity of this will be evaluated in the future and a 2-D analysis of the circumferential temperature on the tube sections may be investigated based on the findings of the experimental work. This will increase the complexity of the model as the internal and external heat transfer to the fluids will vary on the circumference altering the fluid properties.

Acknowledgements

The author would like to thank the mechanical workshop at Stellenbosch University for the construction of the experimental test receiver, and the NRF for funding this research and making it possible. The author thanks the Centre for Renewable and Sustainable Energy Studies (CRSES) at Stellenbosch University for funding to attend the conference.

References

- [1] Kretzschmar, H. (2014). the Hybrid Pressurized Air Receiver (HPAR) for Combined Cycle Solar Thermal Power Plants, (March). Retrieved from <http://scholar.sun.ac.za>
- [2] Heller, L. (2017) Development of a Dual-Pressure Air Receiver System for the SUNDISC Cycle. Stellenbosch University. Available at: <http://scholar.sun.ac.za/handle/10019.1/101315>.
- [3] D.G. Kröger, (2012), SUNSPOT - The Stellenbosch University Solar Power Thermodynamic cycle, Technical report, University of Stellenbosch
- [4] Sarada, S. N., Raju, A. S. R., Radha, K. K., & Sunder, L. S. (2011). Enhancement of heat transfer using varying width twisted tape inserts. *International Journal of Engineering, Science and Technology*, 2(6), 107–118. <https://doi.org/10.4314/ijest.v2i6.63702>
- [5] Final Report - SOLHYCO (Solar-Hybrid Power and Cogeneration Plants). (n.d.).
- [6] Duffie, J.A. and Beckman, W.A. (2006). *Solar Engineering of Thermal Processes*, vol. 53. Wiley. ISBN 0471698679.
- [7] Blanco M.J., Mutuberría A., García P, Gastesi R. and Martín V. 2009 Preliminary validation of Tonatiuh SOLARPACES Symposium, Berlin, Germany, 2009
- [8] Amsbeck, L., Buck, R., Heller, P., Jedamski, J., & Uhlig, R. (2008). Development of a tube receiver for a solar-hybrid microturbine system. *Proceedings of 14th SolarPACES Conference, Las Vegas, NV, March*, (November), 4–7.
- [9] Craig, K. J., Gauche, P., Kretzschmar, H. (2013). Optimization of solar tower hybrid pressurized air receiver using CFD and mathematical optimization. *Energy Procedia*, 49(April 2015), 324–333. <https://doi.org/10.1016/j.egypro.2014.03.035>